Peridynamic Modelling of Cracking in TRISO Particles for High Temperature Reactors

T.A. Haynes[1,2], A. Battistini[2], A.J. Leide[3,4], D. Liu[4], L. Jones[2,5], D. Shepherd[5] & M.R. Wenman[2]*

[1] School of Engineering, University of East Anglia, Norwich Research Park, Norwich, Norfolk, NR4 7TJ

[2] Department of Materials & Centre for Nuclear Engineering, Imperial College London, Exhibition Road, London, SW7 2AZ

[3] United Kingdom Atomic Energy Authority, Culham Science Centre, Abingdon, Oxfordshire, OX14 3DB

[4] School of Physics, HH Wills Physics Laboratory, University of Bristol, Tyndall Avenue, Bristol, BS8 1TL

[5]National Nuclear Laboratory (NNL), NNL Preston Laboratory, Springfields Works, Salwick, Preston, Lancashire, PR4 0XJ

Abstract

A linear-elastic computer simulation (model) for a single particle of TRISO fuel has been built using a bond-based peridynamic technique implemented in the finite element code 'Abaqus'. The model is able to consider the elastic and thermal strains in each layer of the particle and to simulate potential fracture both within and between layers. The 2D cylindrical model makes use of a plane stress approximation perpendicular to the plane modelled. The choice of plane stress was made by comparison of 2D and 3D finite element models. During an idealised ramp to normal operating power for a kernel of 0.267 W and a bulk fuel temperature of 1305 K, cracks initiate in the buffer near to the kernel-buffer interface and propagate towards the buffer-iPyC coating interface, but do not penetrate the iPyC and containment of the fission products is maintained. In extreme accident conditions, at around 600% (1.60 W) power during a power ramp at 100% power (0.267 W) per second, cracks were predicted to form on the kernel side of the kernel-buffer interface, opposite existing cracks in the buffer. These were predicted to then only grow further with further increases in power. The SiC coating was predicted to subsequently fail at a power of 940% (2.51 W), with cracks formed rapidly at the iPyC-SiC interface and propagating in both directions. These would overcome the containment to fission gas release offered by the SiC 'pressure vessel'. The extremely high power at which failure was predicted indicates the potential safety benefits of the proposed high temperature reactor design based on TRISO fuel.

Keywords

high temperature reactors, Generation IV, peridynamics, cracks, TRISO, coated particle fuel

Highlights

- Initial irradiation-induced stresses in a TRISO coated fuel particle were simulated using a peridynamics model.
- Cracks formed in the buffer during the initial rise to power.
- Cracks formed in the fuel kernel at around 6 times full power.
- Cracks formed in the SiC 'pressure vessel' layer at around 9-10 times full power.

1 Background

Following a small number of accidents in which nuclear fuel has been severely damaged, there is a desire to move towards fuel cladding technology that is more inherently safe. A number of so-called accident tolerant fuels (ATF) have been proposed for current light water reactor (LWR) reactor designs. These include coated zirconium alloy claddings; FeCrAl claddings; novel pellet materials and SiC-SiC composite cladding [1-14]. Moving to the longer term, advanced technology fuels (also termed ATF) offer the possibility of not only enhanced safety, but the opportunity to move towards higher burnups. Small modular reactors (SMRs) built on a factory-based production line could offer reduced build times and hence financial risk prior to commencement of initial power supply. In addition, SMRs offer the potential for load-following capability as well as higher temperatures giving better thermodynamic efficiency and improved economics [15-24]. They also offer the opportunity for nuclear to move beyond merely providing a baseload generating capacity in the drive for 'net zero'. By providing high temperature heat, the reactors could supply district heating, heat for industrial uses, and heat for hydrogen co-generation [25].

One example of an advanced technology fuel is tristructural-isotropic (TRISO) particle fuel, a micrograph of which is shown in Figure 1. The TRISO particle consists of a uranium-based fuel kernel surrounded by four layers of materials designed to offer fission product retention and structural support [26] with a total diameter of around 1 mm. The fuel kernels have historically been formed of uranium dioxide (UO_2) [27] or uranium oxycarbide (UCO) [15, 28], although uranium nitride (UN) [22] has been suggested as a means of increasing the density of fissile material. The layers encasing the fuel kernel consist of: a porous buffer layer of carbon intended to absorb fission product recoil and accommodate dimensional change; a inner dense pyrolytic carbon (iPyC) layer; a SiC layer to provide strength and act as a barrier to gaseous and metallic fission products [16]; and, a dense outer pyrolytic carbon (oPyC) layer. The iPyC and oPyC layers, at around 90% theoretical density, act as a barrier to species migration and protect the SiC from chemical attack [23]. The three outer layers (iPyC-SiC-oPyC) are termed the TRISO coating [29]. The TRISO particles are then embedded into surrounding graphite / SiC matrix 'compacts' to provide moderation and structural integrity.

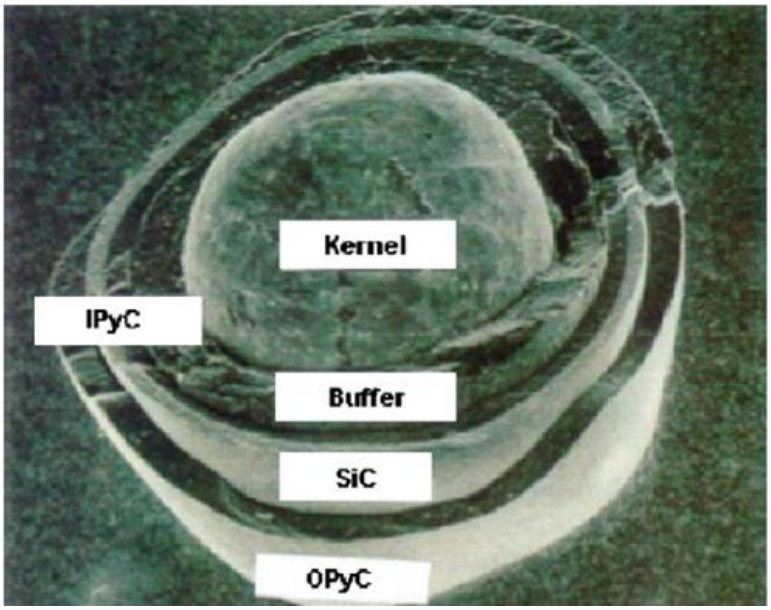


Figure 1 - A micrograph of a TRISO particle. Reproduced from Fig. 1 in [30].

Given that the SiC layer forms the primary barrier against fission product release, most models have been focused on this layer, frequently treating it as a pressure vessel. Li et al. considered the SiC as a rigid pressure vessel, perfectly bonded to the PyC layers [18]. A number of models have been developed that treat the carbon layers as visco-elastic and the SiC layer as purely elastic material [23]. The stress in the SiC is designed to be zero at the start of life. It then becomes compressive due to densification of the PyC layers, reaching the order of 100 MPa at a fast fluence of approximately 0.5×10^{25} n m^{-2} [23]. Due to PyC swelling and the build-up of carbon monoxide and dioxide (CO and CO_2), the stress increases (becomes more tensile) towards the end of life. This has the potential to cause failure if it becomes tensile and greater than the fracture stress [23]. The historic approach is to assume spherical symmetry and solve the mechanics of the particle using closed form 1D analytical solutions [23]. This is analogous to conventional 2D(*r-z*) axisymmetric models for conventional pellet fuel in tubular cladding such as TRANSURANUS and ENIGMA [31, 32].

The most complete 1D model for TRISO fuel performance is PARFUME (**par**ticle **fu**el **m**od**e**l) [19, 33, 34]. In common with other fuel performance codes, PARFUME uses stress concentration factors derived from finite element models to account for a pre-imposed crack. The effect of a crack in the iPyC layer was to change the maximum principal stress in the SiC layer from a compressive stress of around 700 MPa (in the uncracked case) to a tensile stress of 440 MPa (in the cracked case) [33]. A further evolution is to analyse the statistical prediction of failure due to of a number of interacting failure mechanisms which are computationally demanding to capture [35].

The introduction of complicated fracture patterns such as crack coalescence or branching is challenging using techniques such as the extended finite element method (XFEM) [36]. In contrast, peridynamics allows complicated crack patterns to develop naturally. Phenomena such crack initiation, branching and retardation can be predicted as a result of the underlying geometry, material properties and loading. This paper investigates the behaviour of a TRISO fuel particle during early service life using a bond-based peridynamics model implemented in Abaqus. This enables the prediction of the crack patterns within each layer, together with the interaction between cracks in each layer.

2 Methodology

2.1 Peridynamic Modelling in Abaqus

In peridynamics, objects are decomposed into a number of 'material points'. The behaviour of each material point is dependent upon those in a horizon surrounding the material point, not just its nearest neighbours [37]. An example of this is shown Figure 2.

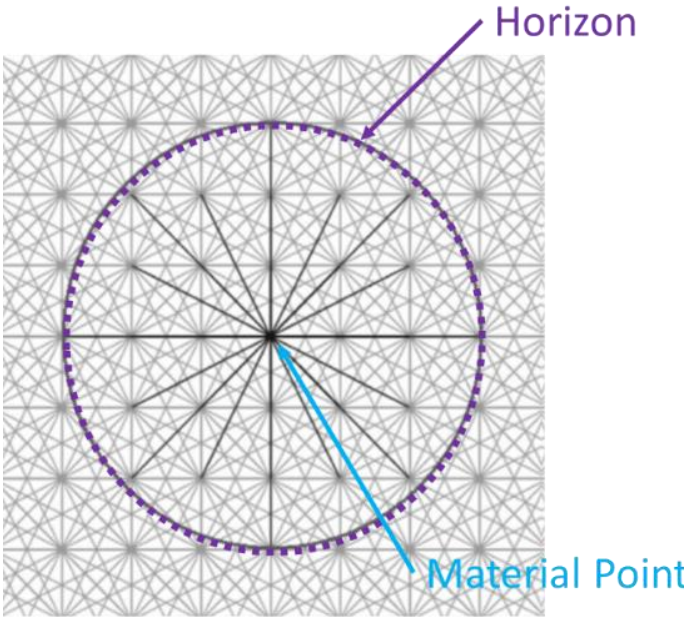


Figure 2 – A material point surrounded by a horizon of other material points. In bond-based peridynamics, bonds connect all of the material points within the horizon. Adapted from Figure 1 in [37].

'State-based' peridynamics uses information about the surrounding material points to determine the response of a material point. This approach has been applied by a number of authors [38], as well as to nuclear fuel more specifically [39-42]. 'Bond-based' peridynamics considers a number of bonds connecting a material point to surrounding material points. It can be readily introduced to a finite element code [37, 43-48] and the full range of material properties available in a finite element model employed. For this reason, a bond-based implementation of peridynamics in Abaqus was chosen for this work.

This work broadly follows the theoretical background, described by Le and Bobaru [49]. In the Abaqus implementation presented here, each 'material point' is represented by a node, and truss elements represent the 'bonds' linking the material points. This approach is discussed in more detail in [37].

2.2 Peridynamic Model for TRISO Particles

Figure 3 shows the model for TRISO particles used to investigate cracking during an idealised power history. Seventy rings of nodes were used across the radius of the particle, giving a nominal nodal separation of 5.6 μm. This gives a total of 15,373 nodes and 211,108 trusses at a horizon ratio of three. At the top, bottom, left and right of the model, the particle is constrained to not move in the azimuthal direction – this prevents spurious rotation. A temperature boundary condition is applied to the whole of the model and the temperature at individual nodes determined using the analytical solution described by equation (17). It should be noted that whilst most finite element models for TRISO particles assume a buffer-iPyC gap, in this work we have not. This is because we wished to predict the debonding and cracking during routine early life.

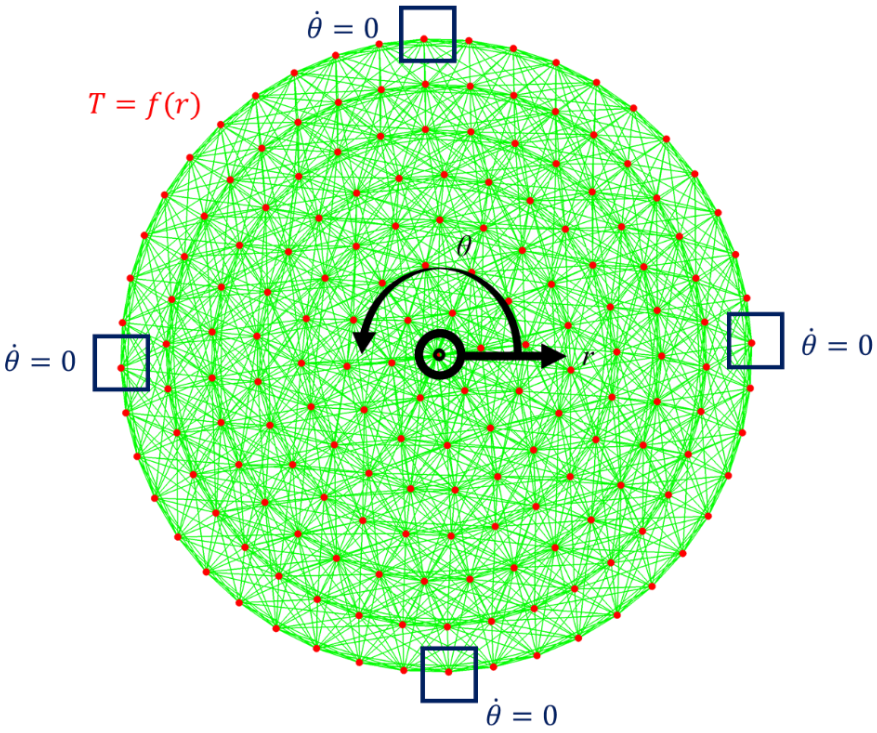


Figure 3 – A schematic for the peridynamic model for TRISO particles used to investigate cracking during an idealised power history. Red 'dots; indicate nodes; green lines indicated bonds; squares represent boundary conditions; and the circle and arrow represents a plane polar co-ordinate system. For clarity, the nodal separation shown in this figure has been increased by a factor of 10 over that used in the simulations, making the mesh 10 times coarser.

The material properties of a bond depend upon the distance of the connected material points from the centre of the fuel kernel. Bonds which cross material interfaces are addressed in Section 2.3. The radius of each region of material are given in Table 1; this was based upon a 'standard' particle with a 350 µm kernel diameter and the layer thicknesses applied in the US AGR-1 and AGR-2 experiments [20].

Table 1 - The outer radius of each region of material of the TRISO fuel particles modelled.

	Thickness of Region (µm)	**Outer Radius of Region (µm)**
UO_2 Kernel	-	175
Buffer	100	275
iPyC	40	315
SiC	35	350
oPyC	40	390

2.3 Bonds Crossing Material Interfaces

For trusses crossing an interface, the assignment of material properties such as the elastic modulus to bonds is somewhat complicated. For example, the macroscopic elastic modulus differs at each end of the bond. In addition, one should bear in mind that the bonds or trusses are modelling constructs and do not exist in the physical sense and are simply carrying forces between material points. In contrast, the nodes represent the material of a given volume surrounding themselves. The material exists and therefore the nodes have a physical meaning.

In this work, the strength of a truss crossing an interface is set to the assumed strength of the interface, given in Table 4. There are however several different ways of assigning an elastic modulus to the trusses. In this work, four approaches were considered:

1. Taking the average elastic modulus of the nodes at each end of the truss.
2. Modelling the truss itself as consisting of two materials with an interface at the midpoint of the truss.
3. Assuming the maximum elastic modulus of the nodes at each end of the truss.
4. Assuming the minimum elastic modulus of the nodes at each end of the truss.

By testing each approach, it was found that using the minimum elastic modulus of the nodes at either end of an interface truss gave the best overall behaviour for all of the interfaces. Employing the minimum elastic modulus also represents the minimum stress. In addition, using the minimum stress would be sensible in the light of Weibull's weakest link theory for brittle fracture [44, 50, 51].

2.4 Material Properties

The approach taken by this work was to use start of life material properties. This involved neglecting the impact of burnup and changes in porosity.

Porosity

The initial fractional porosities were assumed to be 0.010 for the UO_2 kernel; 0.560 for the buffer; 0.160 for iPyC ; 0.006 for SiC and 0.166 for oPyC [52].

Elastic Modulus

The elastic modulus of UO_2, E_{UO2}, as described by MATPRO [53], is given by (1); the units for the elastic modulus are GPa; P is the fractional porosity and T, the absolute temperature in Kelvin. It should be noted that these values were derived for conventional LWR fuel.

$$E_{\mathrm{UO2}} = 233.4(1 - 2.752P)(1 - 1.0915 \times 10^{-4}T) \quad (1)$$

The elastic modulus of the buffer, E_{BUF}, is given [54] by (2).

$$E_{\mathrm{BUF}} = 34.5e^{-2.03P} \quad (2)$$

A number of expressions are available for the elastic modulus of PyC, E_{PyC}, [18, 54, 55]. The simplest, given in (3) and described by Park et al. [55], uses a standard correction term for porosity, originally derived for alumina [56], hence its representativeness of PyC is questionable and thus an area where new data should be sought. Further, it should be noted that this expression does not take into account the anisotropy of PyC; an alternative expression that includes the impact of this is available in [54].

$$E_{\mathrm{PyC}} = 25.0(1 - 1.91P + 0.91P^2) \quad (3)$$

A number of correlations for the elastic modulus of SiC are available in the literature [57]. The relationship recommended by Powers [23], for use in TRISO fuel performance codes, is given by (4).

$$E_{\mathrm{SiC}} = 460e^{-3.57P} - 0.04Te^{-962/T} \quad (4)$$

Poisson's Ratio

In bond-based peridynamics, Poisson's ratio is constrained to 1/3 in plane stress [58] and ¼ in 3D [59] or plane strain [46]. Poisson's ratio was therefore constrained to 1/3 or 1/4, as appropriate in the bond-based peridynamics models; state-based models have no such constraint. For the finite element models, the values given in Table 2 were used.

Table 2 – Poisson's ratio for each material in the finite element model

Material	Value	Source
UO_2	0.32	[60-62]
Buffer	0.23	[54]
PyC	0.33	[18]
SiC	0.21	[57]

Thermal Conductivity

The thermal conductivity of nuclear materials is a function of their burnup, temperature, porosity and level of fission product contamination. A number of correlations for the thermal conductivity of UO_2 are available in the literature and have been discussed in depth elsewhere [63] . The starting point is normally setting the thermal conductivity of irradiated fuel to be the product of the thermal conductivity of unirradiated fuel, k_0, and a number of correction factors. The thermal conductivity of unirradiated fuel [in J K^{-1} m^{-1}] is usually expressed, using (5), as the sum of a phonon term, k_{ph}, [typically a power series in the absolute temperature, T] and an electronic term, k_{el}, [typically a negative exponential of the temperature].

$$k_0 = k_{\mathrm{ph}} + k_{\mathrm{el}} \tag{5}$$

Lucuta's model [64-66] is widely applied in the literature and so is given in more detail as an example. Lucuta's phonon and electronic terms, given by (6) and (7), are based upon the work of Harding & Martin [67].

$$k_{\mathrm{ph}} = \frac{1}{3.75 \times 10^{-2} + 2.165 \times 10^{-4} T} \tag{6}$$

$$k_{\mathrm{el}} = \frac{4.715 \times 10^{9}}{T^2} e^{-1.6361 \times 10^{4}/T} \tag{7}$$

A multiplicative porosity correction factor is given by (8), in which P is the fractional porosity and σ_S a shape function [set to 1.5 for spherical pores]. In this work, it was assumed that the fuel porosity was 1.0%.

$$K_{\mathrm{P}} = \frac{1 - P}{1 + (\sigma_{\mathrm{S}} - 1)P} \tag{8}$$

In the peridynamic models, the average thermal conductivity was determined in a user-defined sub-routine and used to determine the temperature profile in the kernel. More details on this approach are given in Section 2.5.

Thermal Expansion

Table 3 gives the coefficient of thermal expansion, α, assumed for each layer in the TRISO particle; all materials were assumed to be isotropic. In the peridynamics model, the total expansion of a truss is determined in the user-defined field subroutine and passed to Abaqus through a field variable. The code was amended to set the expansion as the average of that of the nodes at each end of the truss.

Table 3 – Coefficient of thermal expansion for each material.

Material	*Value* (K^{-1})	Source
UO_2	1.0×10^{-5}	Williamson [68]
Buffer	3.5×10^{-6}	German & UK Data [54]
PyC	5.55×10^{-6}	Average of UK and German Data [54]
SiC	4.9×10^{-6}	Typical value at 1000 °C [24, 57]

Density

A volume-averaged density was determined to be 2.72×10^3 kg m^{-3} and this was applied to the models. Assigning an averaged density to nodes is a simplification and current a limitation of the current pre-processor. The approximation was judged to not have a great influence upon the results given the constraint upon the crack fragments. For instance, in the kernel the mass applied to each material point will be a third of that which it should be. Upon bond failure, elastic energy is converted into kinetic energy in the node. The velocity of the nodes will therefore be underestimated by a factor of $\sqrt{3}$. Work is ongoing to overcome this under-estimate.

Fracture Stress

For a bond entirely within a material, i.e. not near a free surface or material interface, the fracture strength of the bond, $\sigma_{F,Bond}$, will be given by the fracture strength of that material. This is passed to Abaqus through the user-defined field sub-routine. The fracture stresses of each material, or pair of materials in the case of an interface are given in Table 4. The available data is sparse, consisting predominantly of strengths obtained at room temperature. The values used are given in Table 4. Of particular significance is that no data is available on the strength of either the kernel-buffer or buffer-PyC interface. In this work, we have set the strength of these two interfaces to be equal to the average of the materials on either side of the interface. Future work could investigate the appropriateness of this assumption against the backdrop of validation against experimental data.

Table 4 – Material fracture stresses assumed.

Material 1	Material 2	Strength (MPa)	Notes
Kernel	Kernel	150	Fracture strain [69], combined with room temperature elastic modulus
Kernel	Buffer	100	No data – average fracture stress of kernel and buffer used.
Buffer	Buffer	50	Based upon UK data for PyC and a correction for porosity [54]
Buffer	iPyC	150	No data – average fracture stress of buffer and iPyC used.
iPyC	iPyC	250	Average of US and German data in [54]

Material 1	Material 2	Strength (MPa)	Notes
iPyC	SiC	870	Average of the normal and shear values obtained from TRISO particles [17]
SiC	SiC	620	Average of the values provided in [54]
SiC	oPyC	870	Average of the normal and shear values obtained from TRISO particles [17]
oPyC	oPyC	250	Average of US and German data [54]

2.5 Thermal Model for a TRISO Fuel Particle

A temperature boundary condition was applied to all nodes using the user-defined displacement sub-routine; in Abaqus the displacement boundary condition is used to define all degrees of freedom, including temperature. The temperature profile was based upon a simple pseudo-steady-state temperature solution. This relied upon the following two approximations:

- That all regions except for the kernel were held at the same bulk temperature. Effectively the kernel is embedded in an infinite thermal sink. This approximation was made as particles will reside in regions with different temperature gradients across them due to their comparative position in the pellet / pebble / matrix. In addition, the TRISO particles are so small that no significant temperature gradients are expected.
- The thermal conductivity of the kernel varied with temperature, as shown and discussed in Section 2.3. The average thermal conductivity, k_{av}, was then determined This was justified by the comparatively low temperature drop across the kernel and significant computational saving.

Poisson's equation for heat flow in the presence of a volumetric heat flux in W m^{-3}, q, is given by (9), in which k is the thermal conductivity in W m^{-1} K^{-1}, T the temperature in K and ∇^2 the Laplace operator with units m^{-2} [70].

$$\nabla^2 T = -\frac{q}{k} \tag{9}$$

Using spherical polar co-ordinates, assuming an average thermal conductivity, an isotropic heat flux and azimuthal symmetry transforms (9) into (10).

$$\frac{1}{r^2}\frac{d}{dr}\left(r^2\frac{dT}{dr}\right) = -\frac{q}{k_{av}} \tag{10}$$

Integrating once gives (11).

$$r^2\frac{dT}{dr} = -\frac{q}{3k_{av}}r^3 + A \tag{11}$$

At the origin (r = 0), the heat flux is a minimum in order to maintain symmetry. This necessitates setting the integration constant, A, to zero. Equation (11) therefore becomes (12).

$$\frac{dT}{dr} = -\frac{q}{3k_{av}}r \tag{12}$$

Integrating once more gives (13), in which B is a second integration constant.

$$T = -\frac{q}{6k_{av}}r^2 + B \tag{13}$$

Substituting the outer radius of the kernel, R, and the bulk temperature T_{Bulk} into (13) gives (14).

$$T_{Bulk} = -\frac{q}{6k_{av}}R^2 + B \tag{14}$$

This allows B to be determined.

$$B = T_{Bulk} + \frac{q}{6k_{av}}R^2 \tag{15}$$

Substituting (15) back into (13) gives (16)

$$T = -\frac{q}{6k_{av}}r^2 + T_{Bulk} + \frac{q}{6k_{av}}R^2 \tag{16}$$

And so, the temperature profile within the kernel becomes (17).

$$T = T_{Bulk} + \frac{q}{6k_{av}}(R^2 - r^2) \tag{17}$$

2.6 Thermal Boundary Conditions & Loads

The temperature assumed for all materials except the kernel was set to 1305 K at full power. This was based upon the fuel volume averaged temperature reported for AGR-2 [52]. During a single 24-hour step, the temperature of the outside of the kernel was increased linearly from 293 K to 1305 K. This temperature was chosen the reflect the fuel volume averaged temperature in the AGR-2 experiment.

The volumetric heat flux applied to the model was taken from Hu and Uddin [71] and gives a power of 0.267 W (1.19×10^{10} W m^{-3}) for a 350 μm diameter kernel and agrees with the value of 0.3 W used by Rodríguez Garcia et al. [72].

To model extreme events, separate simulations were run in which the kernel was increased to 1000% power (2.267 W) to assess the impact of a severe ramp upon cracking.

2.7 Benchmarking Simulations

In previous work, a 2D(r-θ) slice through a cylindrical pellet waist or section of cladding was used as an approximation, normally under generalised plane strain, to a 3D cylinder [37, 43, 44, 63, 73]. In this work, a 2D(r-θ) model is used to approximate a 3D sphere. Given that an axisymmetric model is not available in the current bond-based peridynamics implementation, it was necessary to pick either a plane strain or plane stress approximation.

Our current implementation of bond-based peridynamics does however give considerable flexibility in that it allows the user to leverage much of the materials modelling capability available within Abaqus. Utilising Abaqus also offers a lower barrier to technique adoption than a bespoke code. The ability to combine finite element and peridynamic regions in order to capture phenomena such as contact is another advantage. It is hoped that by applying peridynamics in 'industry standard' simulation software, it will accelerate commercial acceptance of the technique. Whilst the approach taken here compares favourably with others

[46], one of the downsides of peridynamics compared to other techniques is the considerable computational cost. To avoid this cost, to date, we have applied the technique to 2D models under conditions of both plane strain and plane strain. This is accompanied a restriction in Poisson's ratio to 1/4 or 1/3 respectively. Clearly, the 3D stress state in a TRISO particle would be best captured by an axisymmetric model. This was not an option due to the truss elements available.

To make the most appropriate choice, between plane strain and plane stress models, a number of equivalent finite element models were run using the same boundary conditions and loads as the peridynamics models detailed above. The finite element models run included:

- An axisymmetric model to capture the correct stress state in the particle.
- A plane stress model.
- A plane strain model.
- A plane stress model with the limitation of Poisson's ratio to 1/3, as per bond-based peridynamics.

3 Results & Discussion

3.1 Stress State in TRISO Particles During Idealised Power Histories

Figure 4 gives the maximum principal stress at the end of the ramp to 100% in each of the finite element simulations described in Section 2.3. Use of a plane strain approximation can be discounted due to the significant stress in the SiC layer compared to the surrounding PyC layers; this is not seen in the axisymmetric or plane stress models. The plane stress models can be seen to give more plausible stress results. For example, the peak stress on the inner surface of the buffer was 27 MPa in the axisymmetric model and 21 MPa in the plane stress model, 22% lower. Using a Poisson's ratio of 1/3 in the model, as used in bond-based peridynamics under conditions of plane stress, makes only a small difference. The maximum hoop stress on the inner surface of the buffer was around 4% higher using a uniform Poisson's ratio than a material-specific Poisson's ratio. For context, it should be noted that for an 'engineering' fuel performance code, errors of up to 10% are more than likely to below those due to uncertainties in other parameters such as many of the material properties. Overall, the use of plane stress model with a uniform Poisson's ratio can be argued to be fair, given the absence of a better solution in the peridynamics implementation detailed here. Work is ongoing on developing the implementation to accelerate 3D modelling for future work.

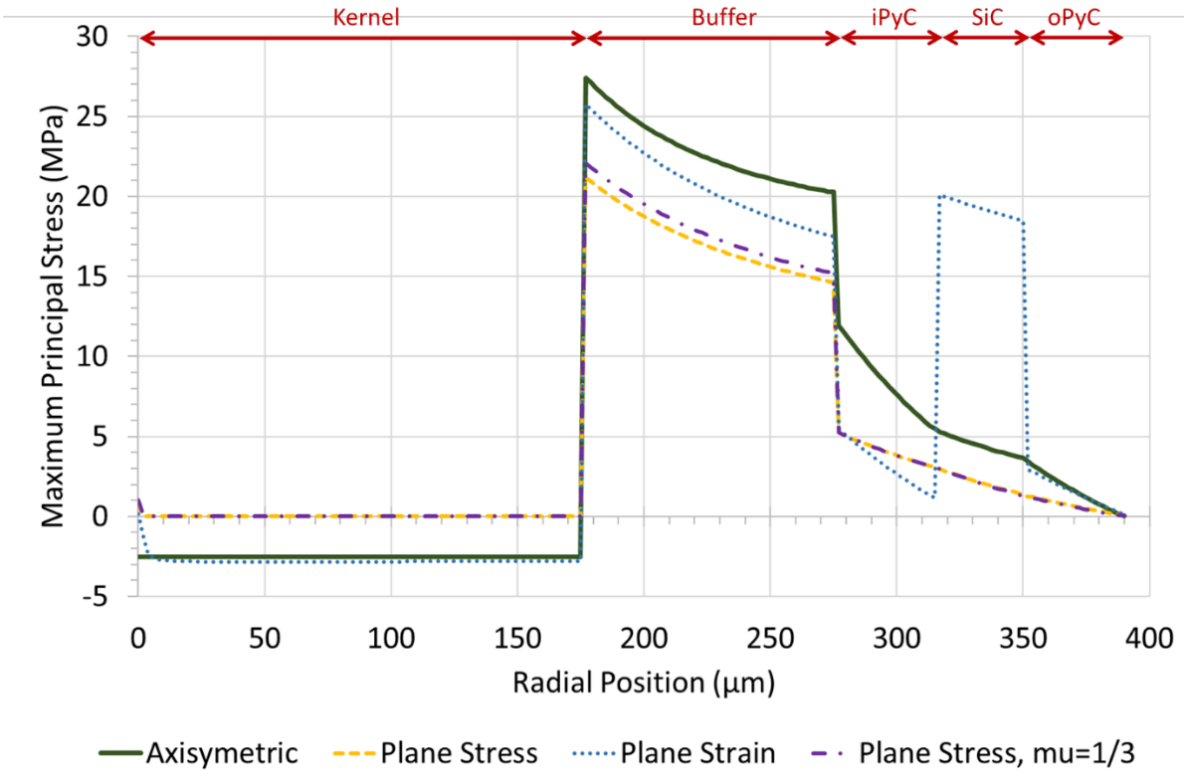


Figure 4 – The maximum principal stress in each of the finite element models described in Section 2.7 at the end of the rise to 100% power.

3.2 Cracking During Rise to 100% Power

The temperature profile in the fuel at the end of the raise to power is shown in Figure 5. The temperature drop across the kernel of 18 K is much lower than seen across the pellets of conventional LWR fuel at the start of life, which is approximately 550 K [68]. The temperature gradient is however similar, at 100 K mm^{-1}, compared to the typical gradient of 140 K mm^{-1} seen in conventional LWR fuel at the same point

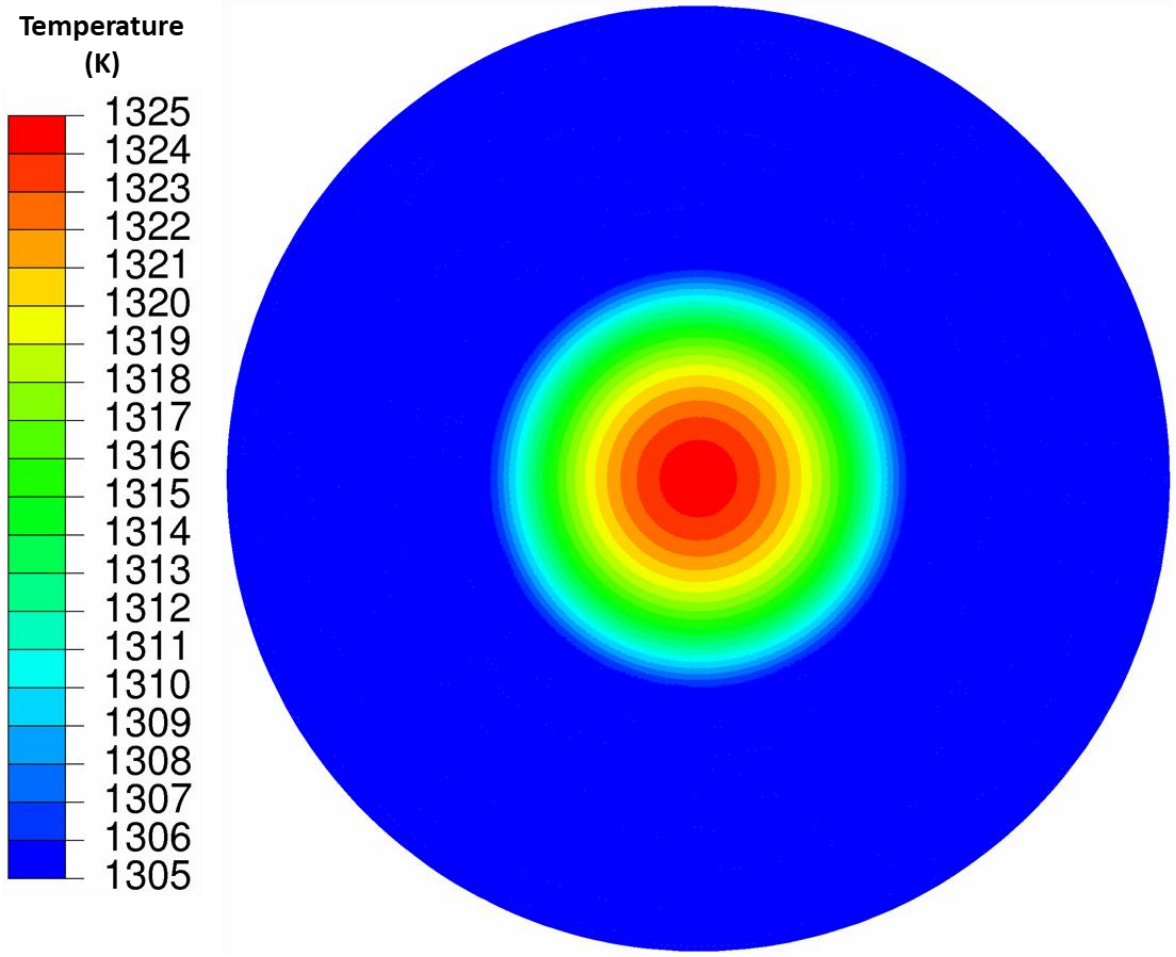


Figure 5 – The temperature in the TRISO particle at the end of the rise to 100% power over 24 hours

Figure 6 shows the fracture pattern in the TRISO particle at the end of a rise to 100% power i.e. normal operation (a kernel power of 0.267 W and a temperature of 1305 K, as described in Section 2.5) over 24 hours. Twenty cracks initiate in the buffer, close to the kernel-buffer interface and around half of these extend outwards radially. They do not however initiate damage in the over-lying iPyC or any of the other layers further towards the outer surface. In addition, circumferential damage is seen in the buffer, close to the kernel-buffer interface. Here, a fundamental difference is seen between TRISO and conventional LWR during the initial rise to power. Namely, that the UO_2 was not predicted to crack in the TRISO fuel, whilst it does in conventional LWR fuel [74]. This might offer potential thermal and fission gas release benefits.

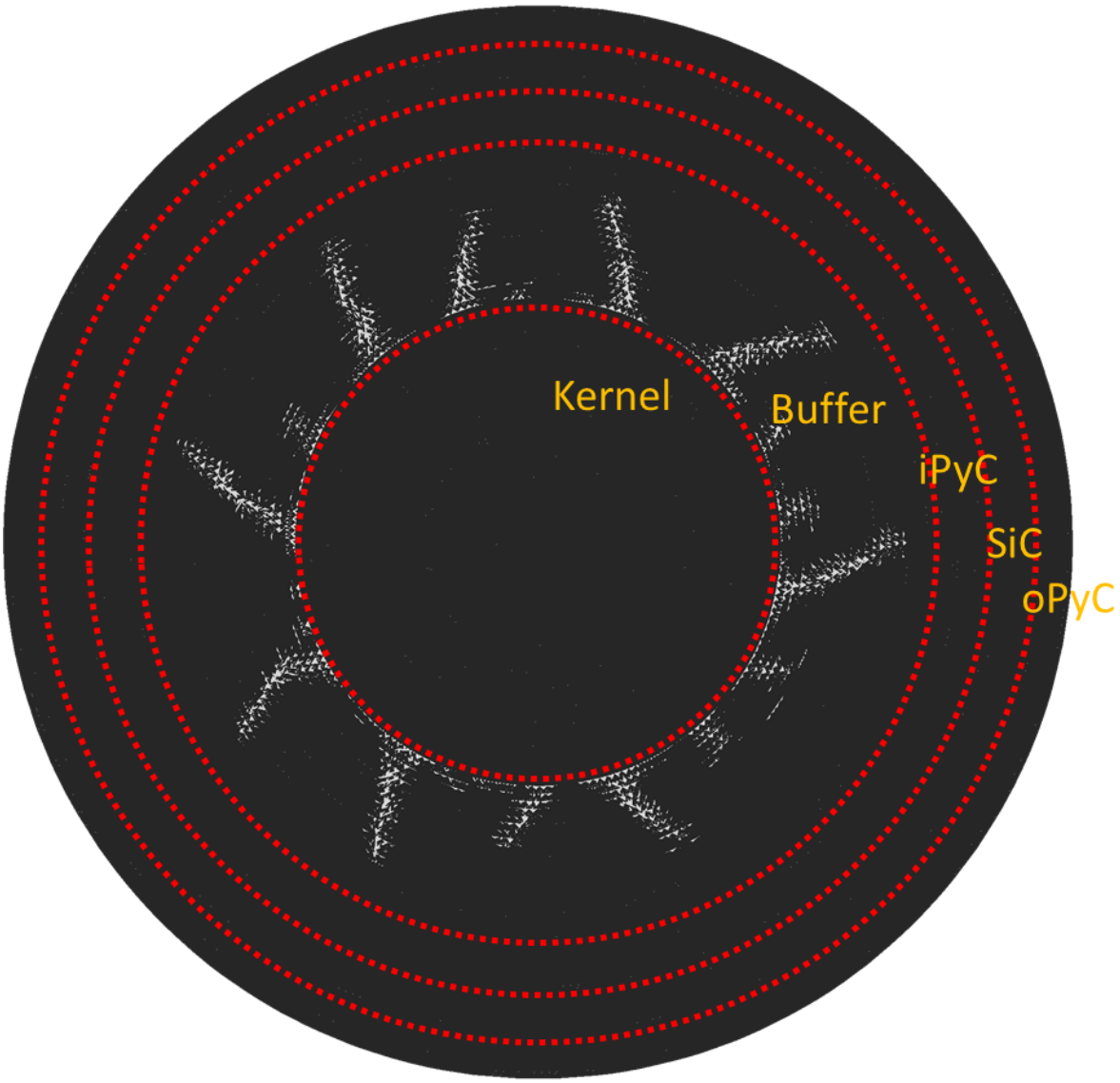


Figure 6 – Fracture patterns in the TRISO particle at the end of the rise to 100% power over 24 hours. Red lines define the layer boundaries and white donates bond failure, a surrogate for damage / cracking.

Figure 7 shows the percentage power at the end of each increment and demonstrates one of the advantages of implementing bond-based peridynamics in Abaqus. Namely, that time steps similar to those required for an explicitly integrated solution can be used during periods of rapid crack propagation and implicit time steps in between, when there is no rapid change in the model. The average time increment during the simulation was 37 s, the minimum 4.3 ns and the maximum 1.8 hours. The simulation took 9.5 hours to run on a workstation computer.

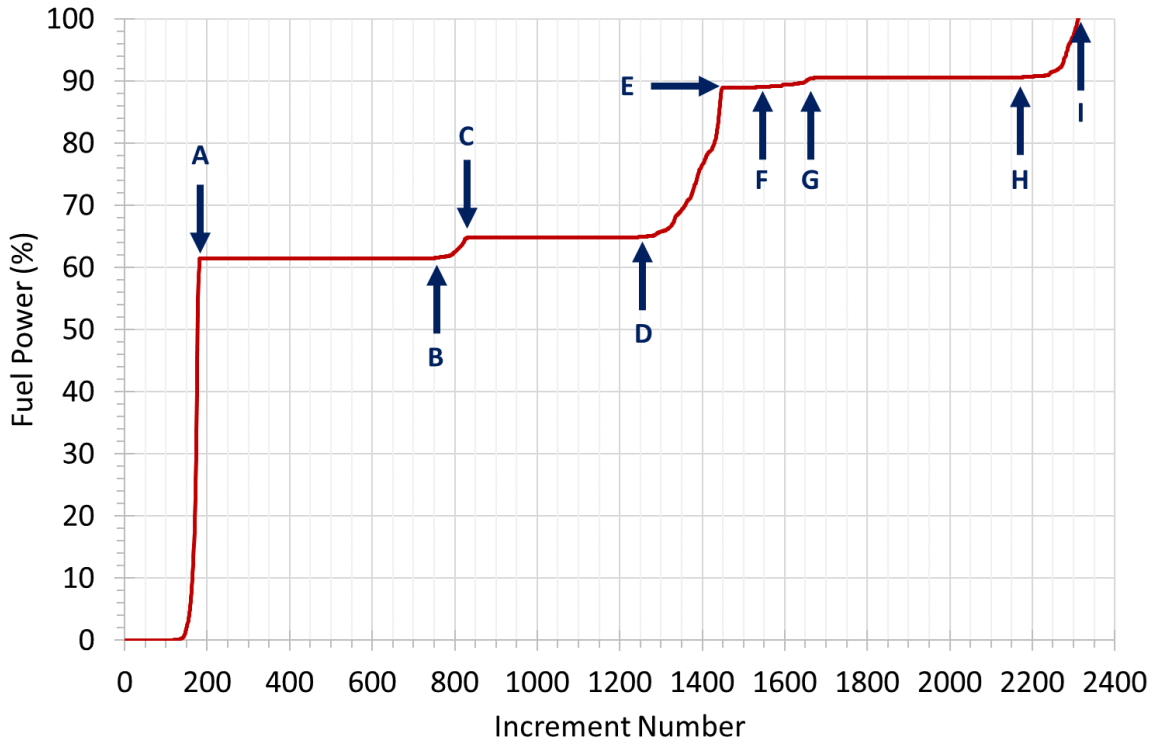


Figure 7 – Incrementation during the simulated rise to 100% power (0.267 W kernel power) over 24 hours. Increment duration ranged from 4.3 ns to 1.8 hours. The letters A-I are points of interest, used in Figure 8. It should be noted that the fuel power increases linearly with time.

Figure 8 shows the development of cracking in the buffer at a number of time points indicated in Figure 7. Between 62 and 65% power, there is a period of crack initiation at the kernel-buffer interface (points A to D). This is followed by a period of slow crack growth towards the buffer-iPyC interface (points D to E) until 89-91% power, when additional cracks initiate at the kernel-buffer interface (points E to H). This second period of initiation is followed by a period of slow crack growth towards the buffer-iPyC interface in a smaller subset of cracks (points H to I).

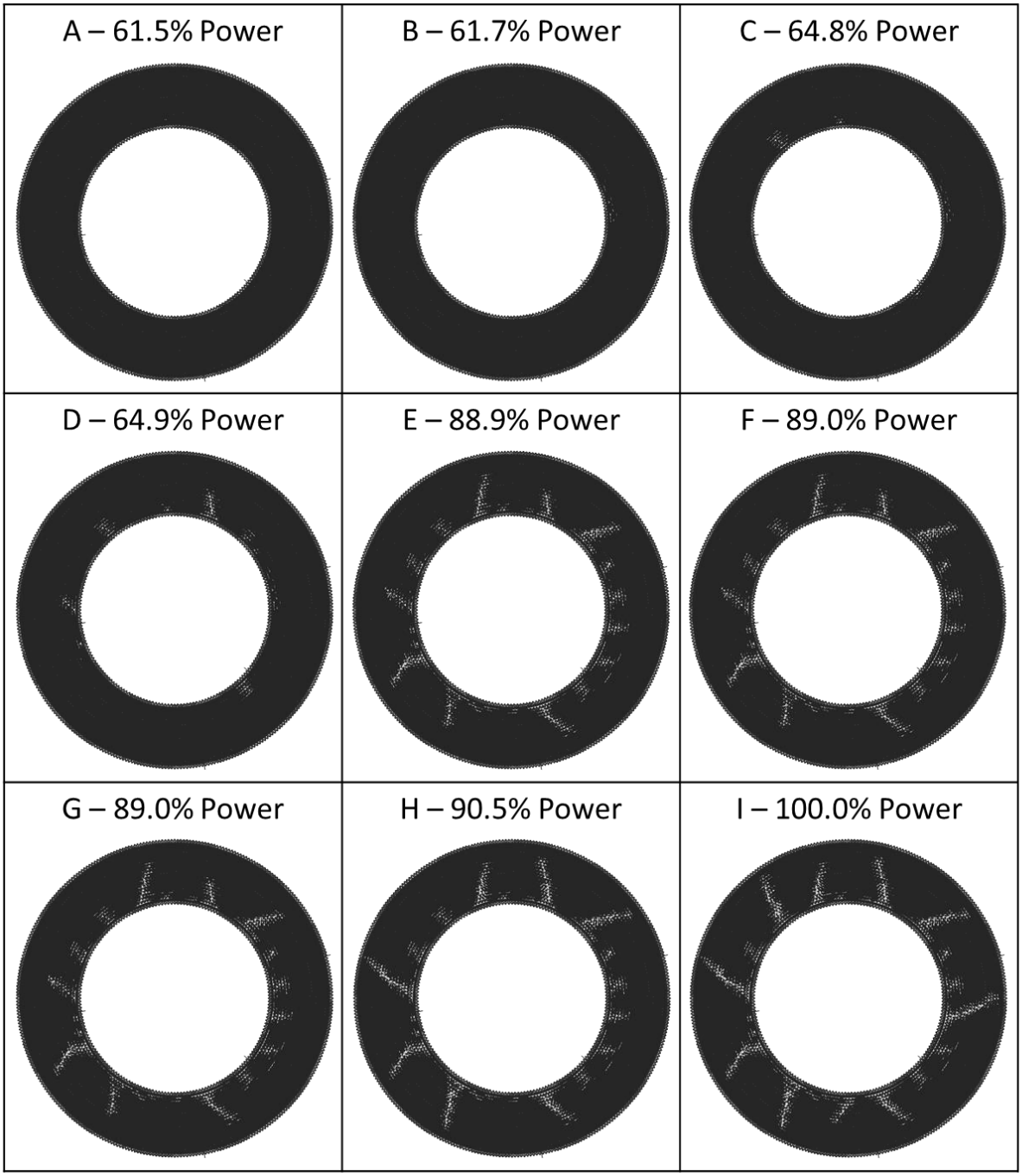


Figure 8 – Crack formation during the rise to full power. The letters A-I are points of interest shown in Figure 7. For clarity, only the buffer region is shown.

3.3 Cracking During Power Ramp

Figure 9 shows the power level reached during the hypothetical extreme power ramp to 1000% power by increment number. In contrast to Figure 7, there are no intermediate stages of periods of rapid cracking, merely the onset of rapid crack growth at 940% power. The very high power required to give rise to cracking in the SiC layer confirms the potential safety advantage of TRISO particle fuel.

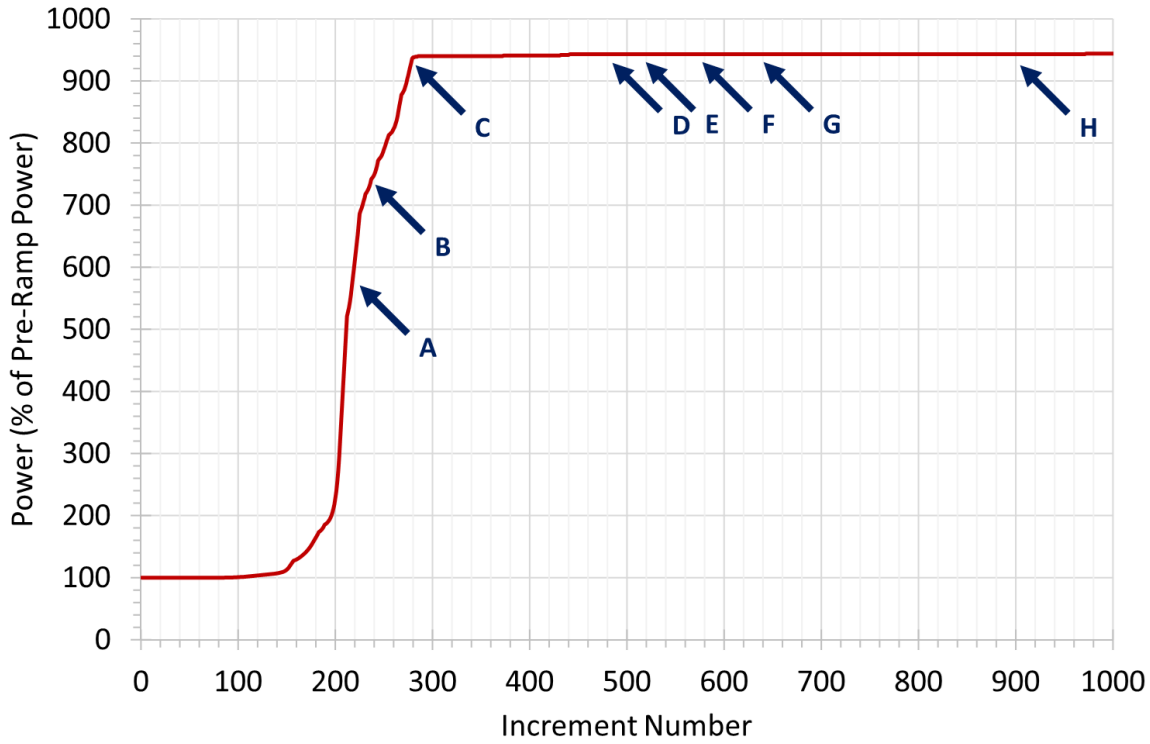


Figure 9 – Incrementation during the simulated power ramp from 100% to 1000% power. Crack patterns at points A to H are shown in Figure 10.

Figure 10 shows the crack patterns at the points A to H shown in Figure 9. At 610% of full power (point A), cracks initiate in the fuel kernel, close to the kernel-buffer interface. These cracks initiate opposite existing cracks in the overlaying buffer. The cracks in the kernel grow slowly (points A to C) until 940% power (point D), when cracks initiate in the SiC at the SiC-PyC interface (points D and E). These cracks increase in number (points F and G) and cracking of the TRISO particle proceeds rapidly towards the outer surface of the SiC layer (point H). It should be noted at point F, the iPyC layer is breached, allowing potential chemical attack of the SiC 'pressure vessel' by fission products. In addition, at point H, the SiC pressure vessel is breached, allowing the egress of fission products, especially gases, from the particle.

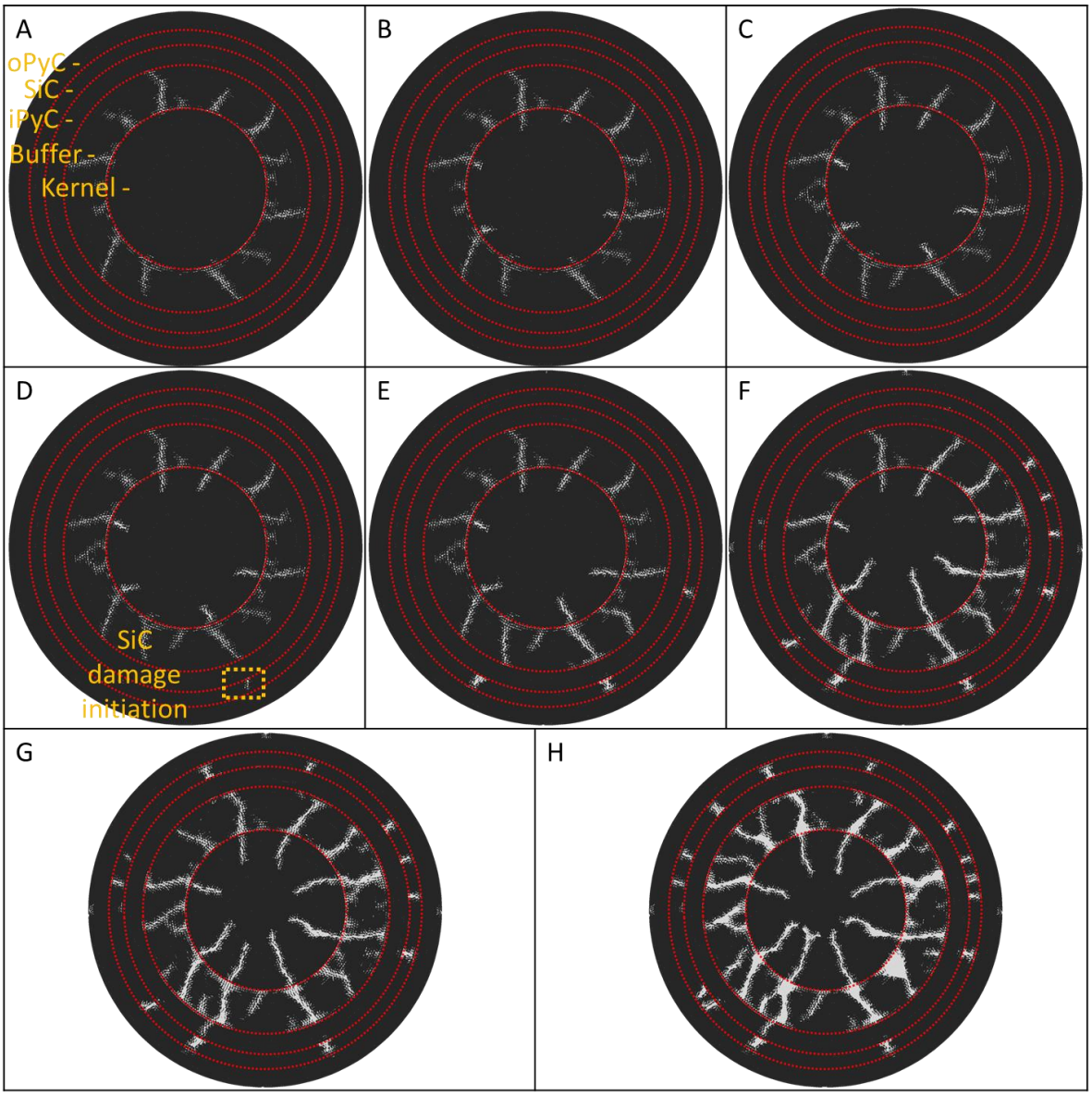


Figure 10 – Crack patterns at the points A to H in the rapid power ramp to 1000% power shown in Figure 9.

3.4 Debonding of the Buffer from Surrounding Layers

Kernel-Buffer Interface

In this work, we have assumed that the kernel and buffer were initially bonded. There is however evidence that immediately following manufacture, the kernel and buffer are de-bonded [75]. This is supported by the observation of debonding post-irradiation [52]. Figure 11(a) is an optical micrograph shows debonding between the buffer and a ZrO_2 kernel manufactured from zirconia, a common surrogate for UO_2. The clean debonding seen experimentally can be reproduced by our model, as shown in Figure 11(b), which shows clean cracking between the buffer and kernel due to a uniaxial load applied in the horizontal direction. The branching crack is likely to be due to post-initiation twisting leading to increasingly mixed mode loading as the crack grows. The impact of residual stresses due to manufacture and the associated cracking of the kernel-buffer interface is clearly something which deserves further research.

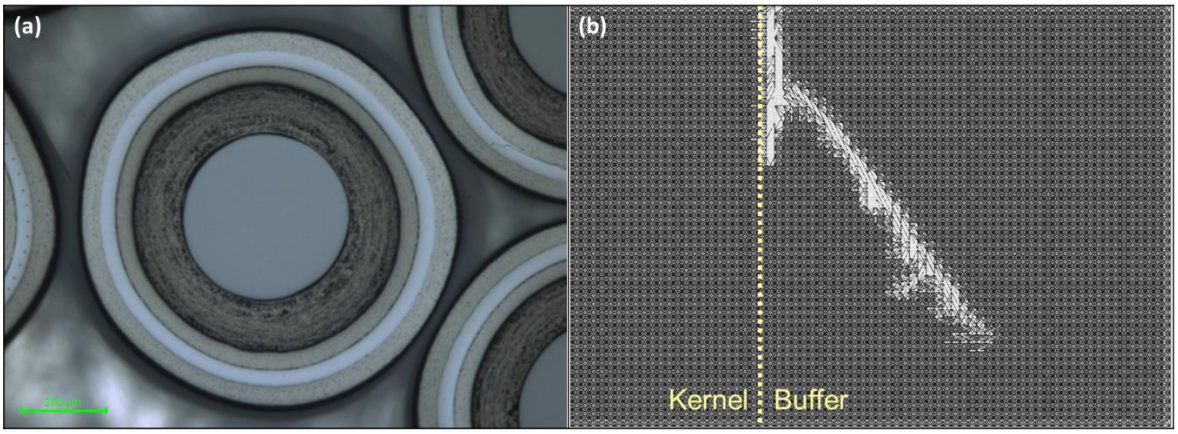


Figure 11 – (a) - An optical micrograph shows debonding between the buffer and a kernel of zirconia in. (b) - Cracking between the buffer and kernel due to a uniaxial load applied in the horizontal direction.

The formation of cracks in SiC opposite those in the underlying iPyC show the value of employing more advanced explicit crack modelling techniques to predict the failure of TRISO particle fuel than those which do not take into account cracks in the underlying layers. The necessity to model cracks in underlying layers is likely to result from the relatively thin nature of the coating layers in a TRISO fuel particle.

Kernel-iPyC Interface

In our work, we did not predict a iPyC-buffer crack, possibly as a result of not modelling irradiation-induced shrinkage and possibly a result of not modelling residual stresses from manufacture. If the buffer and kernel are de-bonded, as has been assumed elsewhere [76], the stress concentration in the kernel might not be as large and so the crack might not 'jump' from one material to the other. This in turn, might reduce the stress concentration in the SiC, again analogous to the situation observed in conventional pellet-clad interaction [77]. We are currently working to implement both residual stress and irradiation-induced shrinkage in our model.

4 Conclusions

In this work, we have developed a 2D linear-elastic peridynamic model for TRISO particle fuel during the initial rise to power. This has shown that:

- In the absence of the capability to carry out an axisymmetric simulation, the most appropriate 2D approximation to the 3D solution for a volumetrically heated sphere is plane stress.
- During an idealised raise to power for a fuel kernel power of 0.267 W and a bulk fuel temperature of 1305 K, cracks initiate in the buffer near to the kernel-buffer interface and propagate radially outwards towards the buffer-iPyC interface. The cracks do not fully penetrate the buffer layer during normal operation.
- During a hypothetical accident involving a power ramp from 100% power (0.267 W) at 0.267 W s^{-1}, cracks formed on the kernel side of the kernel-buffer interface at 610% power. These were opposite existing cracks in the buffer. The cracks in the kernel then propagated slowly.
- The TRISO particle failed at a power of 940%, with numerous cracks rapidly formed at the iPyC-SiC interface, propagating in both directions. During this hypothetical accident, these would overcome the containment to fission gas release offered by the SiC 'pressure vessel'. However, this very high resistance to an extreme power ramp compared to other fuel forms, confirms the potential inherent accident tolerance of coated particle fuel.

Acknowledgements

The authors acknowledge financial support from the UK's Advanced Fuel Cycle Programme (AFCP), funded by the government Department of Business, Energy and Industrial Strategy.

Part of the research presented in this paper was carried out on the High Performance Computing Cluster supported by the Research and Specialist Computing Support service at the University of East Anglia.

References

[1] W. Li and K. Shirvan, "ABAQUS analysis of the SiC cladding fuel rod behavior under PWR normal operation conditions," *Journal of Nuclear Materials*, vol. 515, pp. 14-27, 2019, doi: 10.1016/j.jnucmat.2018.12.017.

[2] Y. He, K. Shirvan, Y. Wu, and G. Su, "Integrating a multi-layer deformation model in FRAPTRAN for accident Tolerant fuel analysis," *Annals of Nuclear Energy*, vol. 133, pp. 441-454, 2019.

[3] "State-of-the-Art Report on Light Water Reactor Accident-Tolerant Fuels," *Nuclear Energy Agency - Organisation for Economic Co-operation and Development*, 2018, doi: https://doi.org/https://doi.org/10.1787/9789264308343-en.

[4] M. Wagih, B. Spencer, J. Hales, and K. Shirvan, "Fuel performance of chromium-coated zirconium alloy and silicon carbide accident tolerant fuel claddings," *Annals of Nuclear Energy*, vol. 120, pp. 304-318, 2018, doi: 10.1016/j.anucene.2018.06.001.

[5] K. A. Terrani, "Accident tolerant fuel cladding development: Promise, status, and challenges," *Journal of Nuclear Materials*, vol. 501, pp. 13-30, 2018.

[6] T. Koyanagi and Y. Katoh, "Mechanical properties of SiC composites neutron irradiated under light water reactor relevant temperature and dose conditions," *Journal of Nuclear Materials*, vol. 494, pp. 46-54, 2017, doi: 10.1016/j.jnucmat.2017.07.007.

[7] S. Ray, "Accident-Tolerent Fuel: Enhancing Safety," *Nuclear News,* vol. November 2017, pp. 44-47, 2017.

[8] V. Angelici Avincola, P. Guenoun, and K. Shirvan, "Mechanical performance of SiC three-layer cladding in PWRs," *Nuclear Engineering and Design,* vol. 310, pp. 280-294, 2016, doi: 10.1016/j.nucengdes.2016.10.008.

[9] H.-G. Kim, Y.-I. Jung, J.-H. Park, D.-J. Park, Y.-H. Koo, and J.-y. Park, "High temperature steam-oxidation behavior of arc ion plated Cr coatings for accident tolerant fuel claddings," *Surface and Coatings Technology,* vol. 280, pp. 256-259, 2015, doi: 10.1016/j.surfcoat.2015.09.022.

[10] J. G. Stone, R. Schleicher, C. P. Deck, G. M. Jacobsen, H. E. Khalifa, and C. A. Back, "Stress analysis and probabilistic assessment of multi-layer SiC-based accident tolerant nuclear fuel cladding," *Journal of Nuclear Materials,* vol. 466, pp. 682-697, 2015, doi: 10.1016/j.jnucmat.2015.08.001.

[11] C. P. Deck *et al.*, "Characterization of SiCeSiC composites for accident tolerant fuel cladding," *Journal of Nuclear Materials,* vol. 466, pp. 667-681, 2015.

[12] S. J. Zinkle, K. A. Terrani, J. C. Gehin, L. J. Ott, and L. L. Snead, "Accident tolerant fuels for LWRs : A perspective," *Journal of Nuclear Materials,* vol. 448, no. 1-3, pp. 374-379, 2014, doi: 10.1016/j.jnucmat.2013.12.005.

[13] S. Bragg-Sitton, "Overview of International Activities in Accident Tolerant Fuel Development for Light Water Reactors," *US Department of Energy Presentation,* vol. IAEA Techn, 2014.

[14] T. Helfer, "Recent improvements of the fuel thermomechanical modelling in the PLEIADES Platform to better simulate accidental transients conditions using the Alcyone fuel performance code," *First Workshop on Research into Nuclear Fuel in Europe and Materials Modeling and Simulation for Nuclear Fuels Workshop Karlsruhe, Germany, November 16th to 18th,* 2015.

[15] C. Marciulescu and A. Sowder, "Uranium Oxycarbide (UCO) Tristructural Isotropic (TRISO) Coated Particle Fuel Performance," *Electric Power Research Institute,* vol. Topical Report EPRI-AR-1 (NP), 2019.

[16] R. Li, B. Liu, and K. Verfondern, "The study of irradiation-induced failure behavior for the TRISO-coated fuel particle in HTGR," *Journal of Nuclear Materials,* vol. 516, pp. 214-227, 2019.

[17] R. L. Seibert, B. C. Jolly, M. Balooch, and D. P. Schappel, "Production and characterization of TRISO fuel particles with multilayered SiC," *Journal of Nuclear Materials,* vol. 515, pp. 215-226, 2019.

[18] R. Li, B. Liu, and C. Tang, "Modification in the stress calculation of PyC material properties in TRISO fuel particles under irradiation," *Journal of Nuclear Science and Technology,* vol. 54, 7, pp. 752-760, 2017.

[19] W. F. Skerjanc, J. T. Maki, B. P. Collin, and D. A. Petti, "Evaluation of Design Parameters for TRISO coated Fuel Particles to Establish Manufacturing Critical Limits Using PARFUME," *Journal of Nuclear Materials,* vol. 469, pp. 66-105, 2016.

[20] T. J. Gerczak, J. D. Hunn, R. A. Lowden, and T. R. Allen, "SiC layer microstructure in AGR-1 and AGR-2 TRISO fuel particles and the influence of its variation on the effective diffusion of key fission products," *Journal of Nuclear Materials,* vol. 480, pp. 257-270, 2016.

[21] B. C. Davis, "Fracture Strength of the SiC Layer in Triso Coated Fuel Particles," *MSc Thesis, Colorado School of Mines,* 2013.

[22] T. M. Besmann, D. Shin, and T. B. Lindemer, "Uranium nitride as LWR TRISO fuel: Thermodynamic modeling of U–C–N," *Journal of Nuclear Materials,* vol. 427, pp. 162–168, 2012.

[23] J. J. Powers and B. D. Wirth, "A review of TRISO fuel performance models," *Journal of Nuclear Materials,* vol. 405, pp. 74-82, 2010.
[24] P. DeMange, J. Marian, M. Caro, and A. Caro, "TRISO-fuel element thermo-mechanical performance modeling for the hybrid LIFE engine with Pu fuel blanket," *Journal of Nuclear Materials,* vol. 405, pp. 144-155, 2010.
[25] J. C. Gauthier, G. Brinkmann, B. Copley, and M. Lecomte, "ANTARES: The HTR/VHTR project at Framatome ANP," *Nuclear Engineering & Design,* vol. 236, pp. 526-533, 2006.
[26] D. A. Petti, J. Buongiorno, J. T. Maki, R. R. Hobbins, and G. K. Miller, "Key differences in the fabrication, irradiation and high temperature accident testing of US and German TRISO-coated particle fuel, and their implications on fuel performance," *Nuclear Engineering & Design,* vol. 222, pp. 281–297, 2003.
[27] K. Minato, T. Ogawa, K. Fukuda, M. Shimizu, Y. Tayama, and I. Takahashi, "Fission product behavior in Triso-coated UO_2 fuel particles," *Journal of Nuclear Materials,* vol. 208, pp. 266-281, 1994.
[28] J. W. McMurray, T. B. Lindemer, N. R. Brown, T. J. Reif, R. N. Morris, and J. D. Hunn, "Determining the minimum required uranium carbide content for HTGR UCO fuel kernels," *Annals of Nuclear Energy,* vol. 104, pp. 237–242, 2017.
[29] R. N. Morris, D. A. Petti, D. A. Powers, and B. E. Boyack, "TRISO-Coated Particle Fuel Phenomenon Identification and Ranking Tables (PIRTs) for Fission Product Transport Due to Manufacturing, Operations, and Accidents," *U.S. Nuclear Regulatory Commission Office of Nuclear Regulatory Research,* vol. NUREG/CR-6844, 2004.
[30] K. Sawa and K. Minato, "An Investigation of Irradiation Performance of High Burnup HTGR Fuel," *Journal of Nuclear Science and Technology,* vol. 36, no. 9, pp. 781-791, 1999.
[31] K. Lassmann, "TRANSURANUS: a fuel rod analysis code ready for use," *Journal of Nuclear Materials,* vol. 188, pp. 295-302, 1992, doi: 10.1016/0022-3115(92)90487-6.
[32] P. A. Jackson, J. A. Turnball, and R. J. White, "Enigma fuel performance code," *Nuclear Energy,* vol. 29, 2, pp. 107-114, 1990.
[33] G. K. Miller, D. A. Petti, and J. T. Maki, "Development of an Integrated Performance Model for TRISO-Coated Gas Reactor Particle Fuel," *HTR-2002: Conference on high temperature reactors; Petten (Netherlands); 22-24 Apr 2002,* pp. 695-700, 2002.
[34] G. K. Miller, D. A. Petti, J. T. Maki, and D. L. Knudson, "Current Capabilities of the Fuel Performance Modeling Code PARFUME," *HTR-2004: 2nd International Topical Meeting on High Temperature Reactor Technology, Beijing, China (September 22–24, 2004),* vol. INEEL/CON--04-02240, 2004.
[35] S. L. N. Dhulipala *et al.*, "Accelerated statistical failure analysis of multifidelity TRISO fuel models," *Journal of Nuclear Materials,* vol. 563, 2022, Art no. 153604.
[36] J. Zhao, H. Tang, and S. Xue, "Peridynamics versus XFEM: a comparative study for quasistatic crack problems," *Frontiers of Structural and Civil Engineering,* vol. 12, no. 4, pp. 548–557, 2018.
[37] T. A. Haynes, D. Shepherd, and M. R. Wenman, "Preliminary Modelling of Crack Formation and Propagation in SiC / SiC Accident-Tolerant Fuel during Routine Operational Transients using Peridynamics," *Journal of Nuclear Materials,* vol. 540, 2020, Art no. 152369.
[38] G. Hattori and J. Trevelyan, "A Non-Ordinary State Based Peridynamics Implementation for Anisotropic Materials," *Proceedings of the 25th UKACM Conference on Computational Mechanics, 12 - 13 April 2017, Birmingham, United Kingdom,* pp. 106-109, 2017.

[39] R. Mella and M. R. Wenman, "Modelling explicit fracture of nuclear fuel pellets using peridynamics," *Journal of Nuclear Materials,* vol. 467, pp. 58-67, 2015, doi: 10.1016/j.jnucmat.2015.08.037.
[40] Y. Wang, X. Zhou, and M. Kou, "Peridynamic investigation on thermal fracturing behavior of ceramic nuclear fuel pellets under power cycles," *Ceramics International,* vol. 44, pp. 11512-11542, 2018.
[41] S. Oterkus and E. Madenci, "Peridynamic Modeling of Fuel Pellet Cracking," *Engineering Fracture Mechanics,* vol. 176, pp. 23-37, 2017.
[42] J. D. Jones, T. A. Haynes, G. Rossiter, and M. R. Wenman, "Application of Weibull Fracture Strength Distributions to Modelling Crack Initiation Behaviour in Nuclear Fuel Pellets Using Peridynamics," *Journal of Nuclear Materials,* vol. 572, 2022, Art no. 154087.
[43] A. Bamgboye, T. A. Haynes, and M. R. Wenman, "Predicting crack patterns in SiC-based cladding for LWR applications using peridynamics," *Structural Integrity Procedia,* vol. 28, pp. 1520–1535, 2020.
[44] L. D. Jones, L. J. Vandeperre, T. A. Haynes, and M. R. Wenman, "Modelling of Weibull Distributions in Brittle Solids Using 2-Dimensional Peridynamics," *Structural Integrity Procedia,* vol. 28, pp. 1856–1874, 2020.
[45] T. A. Haynes and M. R. Wenman, "Development of a Peridynamic Material Model for Accident-Tolerant Silicon Carbide – Silicon Carbide Pressurised Water Reactor Cladding " *Report for the National Nuclear Laboratory, Version 4, June 2019*, 2019.
[46] R. W. Macek and S. A. Silling, "Peridynamics via finite element analysis," *Finite Elements in Analysis and Design,* vol. 43, no. 15, pp. 1169-1178, 2007, doi: 10.1016/j.finel.2007.08.012.
[47] R. Beckmann, R. Mella, and M. R. Wenman, "Mesh and timestep sensitivity of fracture from thermal strains using peridynamics implemented in Abaqus," *Computer Methods in Applied Mechanics and Engineering,* vol. 263, pp. 71-80, 2013, doi: 10.1016/j.cma.2013.05.001.
[48] B. Kilic and E. Madenci, "Coupling of peridynamic theory and the finite element method," *Journal of Mechanics of Materials and Structures,* vol. 5, no. 5, pp. 707-733, 2012.
[49] Q. V. Le and F. Bobaru, "Surface corrections for peridynamic models in elasticity and fracture," *Computational Mechanics,* vol. 61, no. 4, pp. 499-518, 2018, doi: https://doi.org/10.1007/s00466-017-1469-1.
[50] L. D. Jones, L. J. Vandeperre, T. A. Haynes, and M. R. Wenman, "Theory and Application of Weibull Distributions to 1D Peridynamics for Brittle Solids," *Computer Methods in Applied Mechanics and Engineering,* vol. 363, 2020, Art no. 112903.
[51] W. Weibull, "A Statistical Distribution Function of Wide Applicability," *Journal of Applied Mechanics,* vol. 18, no. 3, pp. 293-297, 1951.
[52] P. A. Demkowicz, D. A. Petti, K. Sawa, J. T. Maki, and R. R. Hobbins, "TRISO-Coated Particle Fuel Fabrication and Performance," *Comprehensive Nuclear Materials (Second Edition),* vol. 5, pp. 256-333, 2020.
[53] L. J. Siefken, E. W. Coryell, E. A. Harvego, and J. K. Hohorst, "MATPRO - A Library of Materials Properties for Light-Water-Reactor Accident Analysis," *Idaho National Engineering and Environmental Laboratory,* 2001.
[54] D. Petti, P. Martin, M. Phélip, and R. Ballinger, "Development Of Improved Models And Designs For Coated-Particle Gas Reactor Fuels," *Idaho National Engineering and Environmental Laboratory Bechtel BWXT Idaho, LLC,* vol. INEEL/EXT-05-02615, 2004.

[55] K. H. Park, J. Y. Park, J. H. Park, W. J. Kim, C. H. Jung, and Y. W. Lee, "A Novel Approach to the Porosity Evaluation of Pyrolytic Carbon Layers in TRISO-coated Fuel," *Transactions of the Korean Nuclear Society Spring Meeting. Chuncheon, Korea, May 25-26 2006,* 2006.

[56] R. L. Coble and W. D. Kingery, "Effect of Porosity on Physical Properties of Sintered Alumina," *Journal of the American Ceramic Society,* vol. 39, no. 387-385, 11, 1956.

[57] L. L. Snead, T. Nozawa, Y. Katoh, T. S. Byun, S. Kondo, and D. A. Petti, "Handbook of SiC properties for fuel performance modeling," *Journal of Nuclear Materials,* vol. 371, pp. 329-377, 2007.

[58] Y. D. Ha and F. Bobaru, "Studies of dynamic crack propagation and crack branching with peridynamics," *International Journal of Fracture,* vol. 162, pp. 229–244, 2010.

[59] Y. H. Bie, Z. M. Liu, H. Yang, and X. Y. Cui, "Abaqus implementation of dual peridynamics for brittle fracture," *Computational Methods in Applied Mechanics and Engineering,* vol. 372, 2020, Art no. 113398.

[60] R. A. Wolfe and S. F. Kaufman, "Mechanical Properties Of Oxide Fuels," *Bettis Atomic Power Laboratory, U. S. Atomic Energy Commission,* vol. WAPD-TM-587, 1967.

[61] R. G. Munro, "Elastic Moduli Data for Polycrystalline Oxide Ceramics," *Materials Science and Engineering Laboratory, National Institute of Standards and Technology,* vol. NISTIR 6853, 2002.

[62] A. K. Sengupta *et al.*, "Some Important Properties of Simulated UO_2 Fuel," *BARC/1999/E/008,* 1999.

[63] T. A. Haynes, J. H. Shea, J. A. Ball, and M. R. Wenman, "Finite element modelling of pellet-clad interaction during operational transients," *TopFuel 2015 Conference Proceedings - European Nuclear Society,* 2015.

[64] P. G. Lucuta, H. J. Matzke, and I. J. Hastings, "A pragmetic approach to modelling thermal conductivity of irradiated UO2 fuel: review and recommendations," *Journal of Nuclear Materials,* vol. 1996, no. 232, 1996.

[65] P. G. Lucuta and H. J. V. Matzke R.A, "Thermal conductivity of hyperstoichiometric SIMFUEL," *Journal of Nuclear Materials,* vol. 223, pp. 51-60, 1995.

[66] P. G. Lucuta and H. J. V. Matzke R.A, "Modelling of UO2-based SIMFUEL thermal conductivity: The effect of the burnup," *Journal of Nuclear Materials,* vol. 217, pp. 279-286, 1994.

[67] J. H. Harding and D. G. Martin, "A recommendation for the thermal conductivity of UO_2," *Journal of Nuclear Materials,* vol. 166, pp. 223-226, 1989.

[68] R. L. Williamson, "Enhancing the ABAQUS thermomechanics code to simulate multipellet steady and transient LWR fuel rod behavior," *Journal of Nuclear Materials,* vol. 415, no. 1, pp. 74-83, 2011, doi: 10.1016/j.jnucmat.2011.05.044.

[69] R. L. Williamson and D. A. Knoll, "Simulating Dynamic Fracture in Oxide Fuel Pellets Using Cohesive Zone Models," *20th International Conference on Structural Mechanics in Reactor Technology (SMiRT 20), Espoo, Finland, August 9-14,* vol. 3, 2009.

[70] K. F. Riley, M. P. Hobson, and S. J. Bence, "Mathematical Methods for Physics and Engineering," *Cambridge University Press,* vol. Second Edition, 2002.

[71] J. Hu and R. Uddin, "3D Thermal Modeling of TRISO Fuel Coupled with Neutronic Simulation," *International Congress on Advances in Nuclear Power Plants,* vol. LA-UR-10-00442, 2010.

[72] L. P. Rodríguez Garcia, D. M. Pérez, C. R. G. Hernández, D. E. Milian Lorenzo, and C. A. Brayner de Oliveira Lira, "Development of a Methodology for yhe Evaluation of the Thermomechanical Behavior of the TRISO Fuel," *2017 International Nuclear Atlantic Conference - INAC 2017, Belo Horizonte, Brazil, 22-27 October 2017,* 2017.

[73] T. A. Haynes, J. A. Ball, and M. R. Wenman, "Modelling the Role of Pellet Relocation in the (r-θ) Plane Upon Pellet-Clad Interaction in Advanced Gas Reactor Fuel," *Nuclear Engineering & Design,* vol. 314, pp. 271-284, 2017.
[74] M. Oguma, "Cracking and Relocation Behaviour of Nuclear Fuel Pellets During Rise to Power," *Nuclear Engineering and Design,* vol. 76, pp. 35-45, 1983.
[75] T. Lowe *et al.*, "Microstructural analysis of TRISO particles using multi-scale X-ray computed tomography," *Journal of Nuclear Materials,* vol. 461, pp. 29–36, 2015.
[76] C. Zhang *et al.*, "Multidimensional multiphysics modeling of TRISO particle fuel with SiC/ZrC coating using modified fission gas release model," *Annals of Nuclear Energy,* vol. 145, 2020, Art no. 107599.
[77] T. A. Haynes, J. A. Ball, J. H. Shea, and M. R. Wenman, "Modelling pellet-clad mechanical interaction during extended reduced power operation in bonded nuclear fuel," *Journal of Nuclear Materials,* vol. 465, pp. 280-292, 2015, doi: 10.1016/j.jnucmat.2015.05.021.